SAND2019-0549C

A Visual Investigation of CFD-Predicted In-Cylinder Mechanisms that Control First- and Second-Stage Ignition in Diesel Jets

Author, co-author (Do NOT enter this information. It will be pulled from participant tab in MyTechZone)

Affiliation (Do NOT enter this information. It will be pulled from participant tab in MyTechZone)

Abstract

The long-term goal of this work is to develop a conceptual model for multiple injections of diesel jets. The current work contributes to that effort by performing a detailed modeling investigation into mechanisms that are predicted to control 1st and 2nd stage ignition in single-pulse diesel (n-dodecane) jets under different conditions. One condition produces a jet with negative ignition dwell that is dominated by mixing-controlled heat release, and the other, a jet with positive ignition dwell and dominated by premixed heat release.

During 1st stage ignition, fuel is predicted to burn similarly under both conditions; far upstream, gases at the radial-edge of the jet, where gas temperatures are hotter, partially react and reactions continue as gases flow downstream. Once beyond the point of complete fuel evaporation, near-axis gases are no longer cooled by the evaporation process and 1st stage ignition transitions to 2nd stage ignition. At this point, for the positive ignition dwell case, all of the fuel has already been injected and the 2nd stage ignition zone is surrounded by a relatively large mass of premixed gas, which results in the premixed-dominated heat release mentioned above. Conversely, relatively little premixed gas surrounds the 2nd stage ignition zone of the negative ignition dwell case, its small premix charge burns rapidly and the remaining charge is supplied via injection during the heat release process yielding a mixing-controlled dominated heat release.

After end-of-injection, both cases leave a distinct residual jet. Gaining a deep understanding of the aforementioned processes is the purpose of this paper. Understanding how a second pulse of fuel burns when injected into residual jets of different character is the subject of future work.

Introduction

Over the past three decades, diesel fuel injector technologies have provided new capabilities for direct injection of fuel into the combustion chamber in multiple pulses per engine cycle. This new flexibility has added new dimensions to the engine control parameter space, allowing optimizations for fuel economy, emissions, noise, and other factors, that were not previously possible with single-injection-per-cycle approaches. Various implementations and schedules of multiple injection approaches have been researched and/or implemented in production hardware. As reviewed recently [1], injection schedules may include one or more typically small pilot injections preceding a larger main injection, splits of the main injection into multiple pulses, and one or more typically small post injections occurring after the main injection(s).

As described in the review [1], multiple injection approaches can allow many adjustments to engine performance, including: controlling soot, hydrocarbon, nitrogen oxides, and carbon monoxide emissions; reducing combustion noise and/or decreasing the ignition delay; increasing fuel-efficiency; controlling liquid penetration; and increasing exhaust gas temperature and/or altering the HC/CO content in the exhaust gas for management of exhaust gas aftertreatment devices.

Although the practical effects of various multiple injection approaches can be quite desirable in the engine system design process, the in-cylinder chemical and physical mechanisms responsible remain unclear, which impedes combustion system optimization [1]. Certainly, there exists sufficient evidence of interaction between individual injection events for many of the multiple injection strategies, but a phenomenological understanding of how either injection affects the other is far from complete. Proposed interaction mechanisms include: fundamental changes from autoignition-dominated combustion to something resembling flame propagation [2]; decreased fuel–air premixing, and hence, a lower pressure rise-rate and acoustic noise but with increased soot emissions; reduction in overmixing in one injection or the other that then reduces incomplete combustion that results in HC and CO emissions [3]; changes to combustion phasing that affect NOx and BSFC [4,5]; enhanced mixing that reduces soot formation or increases late-cycle oxidation [6]; increased local temperatures that

increase the kinetic rates of soot oxidation [6]; and spatial redistributions of local mixtures [6].

The overall goal of the project supporting the current study is to use experimental and modeling results to gain insight into the phenomenological in-cylinder interactions between multiple injections. For experimental measurements, it is typically difficult to attribute measured in-cylinder species to individual injections, which impedes building a phenomenological understanding. For example, if a multiple injection approach is found to alter the in-cylinder mixing state and hence affect pollutant emissions, it is difficult from fuel concentration measurements alone to attribute the local mixture to fuel remaining in the residual jet (i.e., to gases remaining downstream of the nozzle after EOI) or to fuel delivered by the second injection. Such attributions are currently possible with CFD [7], however, and therefore analysis with CFD is a key tool along with experimental data to gain phenomenological insight.

The specific goal of the current study is to analyze predictions from computer simulations to gain insight into the effects of ignition timing on only the residual jet of the first injection of a multiple injection sequence, into which subsequent jets would penetrate. Hence, the current study considers only the first injection, and focuses on the entire sequence of events that create the residual jet.

Figure 1 illustrates our expectations of important features of the interactions between multiple injections for two different types of ignition for the first injection. Figure 1(a-c) represents stages of a classic burning jet when there are two injections. Figure 1a shows the jet after injecting into air, igniting before the end of injection, and then reaching a quasi-steady jet governed by mixing-controlled combustion. After the first injection, Figure 1b illustrates an upstream jet that is expected to burn in a mixing-controlled fashion, and jet momentum is expected to dissipate, leaving a residual jet downstream of the injector nozzle. The gaseous state downstream of the nozzle now differs when compared to the same location prior to the first injection, therefore, heat release rate and emissions formation characteristics for each injection are expected to differ as well. The second injection enters hotter gas that may contain intermediate-combustion species and alter its ignition characteristics (Figure 1c).

Besides the residual mixture influencing the second-jet combustion characteristics, fuel vapor from the second injection may also alter reaction paths in the residual jet. Figure 1(d-f) illustrates analogous stages for a jet with a partially ignited first injection, for which second-stage ignition does not occur until after the end of the first injection. The residual jet for such a condition (Figure 1e) is much cooler than for the classic quasi-steady diesel jet, having not yet attained second-stage ignition. With cooler mixtures and much different species from partial ignition, the interaction between this residual jet and the subsequent injection (Figure 1e) is expected to be much different than for the classic quasi-steady jet.

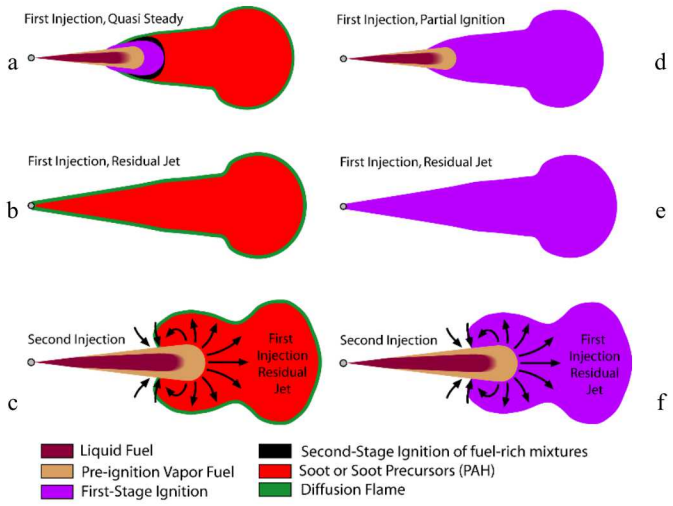

Figure 1. Conjectured phenomenological features expected to be important for multiple injection interactions. Left) First injection developing into classic quasi-steady diesel jet. Right) First injection leading to partially ignited jet.

To simplify the problem as much as possible, we simulate single-injection, free jets into air at engine-like pressures and temperatures, with one jet representative of classic burning jets with second-stage ignition before the end of injection, and the other representative of jets with ignition after the end of injection. The injector, injection schedule, and ambient gas composition and density are identical for the two cases. To vary the ignition delay, the initial ambient temperature is adjusted (and pressure to maintain constant density). Analysis relates the AHRR curve details to predicted transients in jet structure, as well as to pre-ignition, ignition and combustion timings and locations within the jet. Such detail is pursued, because it is these transients that will be interrupted by later injections and will govern the interactions between multiple injections.

A note about color legends used in the figures, scalar values can and often times do extend below and above the legend limits and sometimes by a large amount. For example, the coldest temperature on the color legend might be 500K and colored blue. Then, all locations of the computational domain that are 500K or colder will be colored blue. Similarly, the richest equivalence ratio on its legend might be 4 and colored red. This means that all locations at or richer than 4 will also be red. Actually, due to interpolation between ranges, locations slightly less than 4 will be red as well. The selection of color legend limits is to highlight scalar distributions on the computational domain.

CFD representations and models

In the reacting spray simulations presented herein, injected liquid fuel transitions to vapor, mixes with air and burns. Selecting which computational fluid dynamics (CFD) sub-models are active determines the only possible pathways for these processes. Process representations are given next.

Liquid-spray representation

Groups of physically and chemically identical spherical drops, called parcels, are assigned an initial velocity directed outwardly from a location of the computational domain boundary that represents the injector nozzle location. In aggregate, the parcels represent the penetration and spread of an injected-liquid spray.

Simulated drops are injected into the computational domain within a spreading angle, Equation (1), which is based on the aerodynamic surface wave theory of jet breakup [8]. In essence, the model assigns a velocity component to the parcels, which is perpendicular to the spray axis, causing the spray to spread radially upon injection.

$$\tan\left(\frac{\theta}{2}\right) = C_\theta 4\pi \sqrt{\frac{\rho_g}{\rho_d}}\ f\left(\frac{\rho_d}{\rho_g}\left(\frac{Re_d}{We_d}\right)^2\right) \qquad (1)$$

The model constant, C_θ, depends on injector configuration and nozzle flow. A C_θ value of 0.45 well represents a range of experimental Engine Combustion Network-Spray A data and that value is used in this study as well. See Figure 2 of reference [9] for details.

Parcels push on the chamber gas, which is initially at rest, and displace it in the local-parcel direction. In turn, gases impart a drag on the parcels, which slows them down. Equivalent terms in the parcel and gas momentum equations capture this interaction. Equation (2) is the drag-force model equation [9].

$$\boldsymbol{F}^s = \frac{3}{8}\frac{\rho_g}{\rho_d}\frac{|\boldsymbol{u} + v' - \boldsymbol{v}|}{r_d}(\boldsymbol{u} + \boldsymbol{v}' - \boldsymbol{v})C_d C_{distortion} \qquad (2)$$

$\boldsymbol{u},\ \boldsymbol{v},\ \boldsymbol{v}'$	Gas, parcel, turbulent drop dispersion velocities.
ρ_g, ρ_d	Gas and drop densities.
r_d	Drop radius.
$C_d,\ C_{distortion}$	Drop drag (3) and drop distortion coefficients (4).

$$C_d \quad \begin{matrix} Re_d > 1000 & 0.424 \\ Re_d \le 1000 & 24(1 + 0.17{Re_d}^{0.67})/Re_d \end{matrix} \qquad [10] \qquad (3)$$

$$C_{distortion} \qquad 1 + 2.632y \qquad [11] \qquad (4)$$

Re_d	Drop Reynolds number, $2\rho_g r_d V_{rel}/\mu_g$.
V_{rel}	Relative velocity between drop and gas.
μ_g	Gas viscosity.
y	Drop distortion, $y = f(We_d)$.
We_d	Drop Weber number, $\rho_g r_d {V_{rel}}^2/\sigma_d$.
σ_d	Drop surface tension.

Continuity tends to entrain gas located radially beyond the spray. This ready supply of gas allows the liquid spray to form a jet in and of the ambient gas.

Gaseous-jet representation

Jet theory again, this time with the additional isothermal and non-vaporization assumptions, shows that liquid and gas flowrates in the spray direction have a particular relation, Equation (5).

$$\frac{\dot{m}_d(x)}{\dot{m}_g(x)} = \frac{2}{\sqrt{1 + 16\tilde{x}^2} - 1} \qquad (5)$$

Equation (5) says that for a fixed set of conditions (and assuming that enough gas can be entrained from the surroundings), the ratio of liquid to gas flowrates ($\dot{m}_d/\dot{m}_g$) varies in the spray direction as a function of distance from the injector. The conditions are found in the definition of $\tilde{x}$.

$$\tilde{x} = \frac{x}{x^+} \qquad (6)$$

$$x^+ = \sqrt{\rho_d/\rho_g}\ \sqrt{C_a}\ d/tan(\theta) \qquad (7)$$

x	Coordinate in the spray direction.
ρ_g, ρ_d	Gas and drop densities.
C_a	Area-contraction coefficient.
d	Nozzle diameter.
θ	See Equation (1)

Barring evaporation, the liquid and gas travel downstream (Equation (5)), their relative velocity diminishing with increasing distance from the simulated-nozzle opening due to drag forces (Equation (2)). Gases that are transported downstream through the jet and that reach the jet tip, encounter still-stagnant gas. This interaction deflects gases at the tip radially outward, contributing to the jet's spreading. So jet spreading is a natural occurrence at the downstream tip and is modeled upstream through Equation (1). Modeling improvements to the upstream flow are discussed next.

Practical model for improved near-nozzle momentum exchange – The gas-jet model [12]

Practical applications of engineering CFD simulations typically use grids with computational cell sizes on the order of a millimeter and drops are injected at high speed with drop diameters equal to the nozzle diameter. For this study, the injection-velocity magnitude is ~400 m/s, the initial gas velocity is 0 m/s and injected-drop diameter is 141 µm. Using these values in Equation (2) results in sizeable drag forces near the nozzle.

Sizeable drag forces, alone, are not an issue. An issue arises when drops are injected into a mesh whose computational cells are larger than the parcel's radius of influence. The situation can be understood as follows. The closer an element of gas is to a moving drop, the more it feels the push from the moving drop. Due to dissipation, at some distance the drop motion no longer influences the gas and that distance is called the radius of influence. Note that parcels exchange momentum with the gas occupied by the cell in which they are

located. When cells are larger than the radius of influence, parcels exchange momentum with cells containing excess mass. Therefore, the change in gas velocity due to momentum exchange is under-predicted and the relative velocity used to calculate drop drag ($\boldsymbol{u} + \boldsymbol{v}' - \boldsymbol{v}$ in Equation (2)) remains artificially high, resulting in under-penetration.

The gas-jet model [12] improves momentum-exchange predictions by substituting the CFD-predicted axial velocity, $\boldsymbol{u}$, used in Equation (2), with an axial velocity based on turbulent gas jet theory. As a result, the predicted drag is more in line with experiments and less sensitive to computational cell size as well. Details on the gas-jet model are given in Appendix A.

Vaporization representation

In this study, gas and liquid-fuel drops mix at temperatures sufficient for the liquid fuel to evaporate. Upon evaporation, fuel vapor fills the full volumetric extent of the computational cell holding the parcel and within each cell, fuel vapor and domain gas are co-located, i.e., perfectly mixed at the sub-grid scale. Sharp-species gradients can exist at cell interfaces, the distribution being like patchwork, a fact often disguised by CFD renderings.

The predicted CFD temperature distribution can also be like patchwork. Hot, fuel-lean domain gases are entrained, then cooled by evaporation and gases along the spray axis get colder with increasing penetration until evaporation is complete. Fuel-vapor diffuses in the opposite direction, outward from the axis, and heats up.

In this study, fuel transitions from liquid parcels to fuel vapor in a two-step model process, which is based on experimentally supported assumptions and observations. That is, at high-injection pressure, small drops, about 10 μm diameter, form rapidly, and at this size, temperature gradients within the drops are negligibly small. The drops then reach the local liquid-vapor equilibrium within a typical CFD time step, approximately 1 μs.

These assumptions have interesting model implications. For example, from this viewpoint, an intact-liquid core still exists, so the proven method of initiating near-nozzle sprays by injecting drops with diameters equal to the effective nozzle diameter is still valid and still used. These large drops do become smaller with increasing distance from the injector, but not by instabilities such as surface wave growth, which leads to drop breakup. Instead, liquid fuel is released from these large drops and is tracked as a Eulerian liquid that is collected in each computational cell in which it is released. The Eulerian liquid phase is assumed to be perfectly mixed with the local gaseous phase and is governed by an analogous mass transport equation, Equation (8).

$$\frac{\partial \rho_l}{\partial t} + \nabla \cdot (\rho_l \boldsymbol{u}) = \nabla \cdot \left[\rho \mathrm{D} \nabla \left(\frac{\rho_l}{\rho}\right)\right] + \dot{S}_{EP} + \dot{S}_{release} \qquad (8)$$

ρ_l Mass density of Eulerian liquid.
$\dot{S}_{release}$ Lagrangian drops to Eulerian liquid source term.
$\dot{S}_{EP}$ Eulerian liquid to gas phase-change source term.

Consider the release of fuel from liquid drops to the Eulerian liquid, $\dot{S}_{release}$. Each drop in a parcel starts with an initial mass, call it $m_{d,i}$ and with time drop mass is reduced to a lesser value, call it m_d. At or prior to the liquid length, $x = L$, all of the parcel mass will have been converted to Eulerian liquid (and Eulerian liquid to fuel vapor). A mathematical form for liquid length is expressed by Equation (9)[20].

$$L = C_L \sqrt{\frac{\rho_d}{\rho_g}} \frac{d\sqrt{C_a}}{\tan(\theta/2)} \sqrt{\left(\frac{2}{B(T_g, P_g, T_d)} + 1\right)^2 - 1} \qquad (9)$$

B is the ratio of liquid to gas flowrate at the liquid length, i.e., Equation (5) at x=L, and is a function ambient gas temperature and pressure, and liquid drop temperature T_g, P_g, T_d respectively. Equation (5) can be rearranged to give

$$\gamma(x) = \frac{\dot{m}_g(x)}{\dot{m}_g(L)} = \frac{\sqrt{1 + 16\tilde{x}^2} - 1}{\sqrt{1 + 16(L/x^+)^2} - 1} \qquad (10)$$

Equation (10) is the ratio of the entrained ambient gas mass flowrate at an axial location, x, to the gas mass flowrate at that the liquid length, L, required to totally vaporize the fuel. According to the liquid to gas flowrate relationship of Equation (5), the maximum amount of fuel that can be released is also governed by $\gamma(x)$, such that at any axial location x

$$\dot{S}_{release} = \left(m_p - m_{p,i} \cdot (1 - \gamma(x))\right)/dt \qquad (11)$$

Next consider the conversion of Eulerian liquid to Eulerian vapor, i.e., $\dot{S}_{EP}$ of Equation (8). The solution requires three main components, an equation of state (Peng-Robinson is used), species thermodynamic properties (the DIPPR database is used [21]) and a phase equilibrium solver [22-26]. The solver has been validated extensively for two- and three-phase equilibrium scenarios, for condensation, evaporation, multi-phase dynamic flash and supercritical fluids. With the above mentioned models, along with the CFD solver, KIVA-3V Release 2 [27], Equation (8) is solved.

Chemistry, Turbulence and Computational mesh

Chemical reactions model combustion within the KIVA-3V, Release 2 [27] framework used in this study. A sparse analytical Jacobian chemistry solver [28] solves the n-dodecane reaction mechanism [29] with the standard sub-grid scale, well-mixed assumption. A generalized-RNG k-e turbulence model is used for turbulence modeling [30].

Figure 2 contains specifications of the axi-symmetric mesh. Injection is horizontal from the upper-right corner. The chamber and single-hole injector axes coincide. Near the axis the mesh is more refined in the radial direction. A horizontal line in the figure indicates the location of change in the radial resolution. Results show little mesh sensitivity at this resolution (sensitivity study not documented here). Cells are slightly smaller near the injector (0.21mm radial and 0.16mm axial) and grow by a factor of 1.01 in the radial and axial directions. The figure gives nominal values.

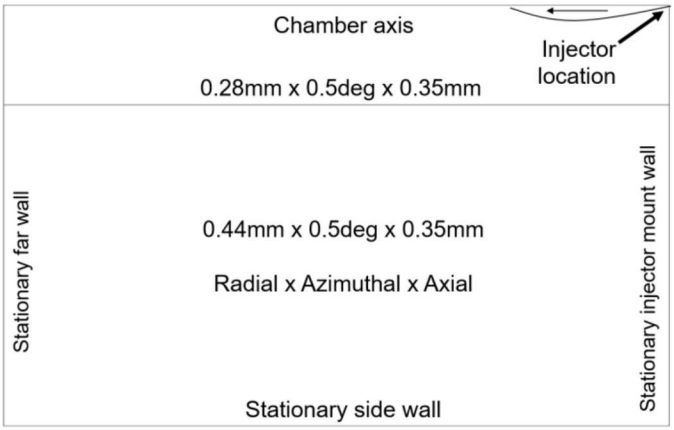

Figure 2. Nominal mesh specifications. Injection is horizontal from the upper-right corner. Mesh is 2D and axi-symmetric.

Apparent heat release rate curves, AHRR, and operating conditions

Negative and positive ignition dwell, referred to as n-dwell and p-dwell respectively, are defined in Figure 3. Ignition dwell is measured with respect to end-of-injection (EOI), and both simulated cases use the same injection profile. For the conditions simulated here, n-dwell and p-dwell ignition are 1ms before and 0.31ms after EOI respectively.

n-dwell AHRR is characterized by:

- A short duration cool flame with low magnitude
- A tall-narrow premixed burn
- A large portion of fuel consumption under mixing-controlled combustion

p-dwell characteristics are nearly opposite with a longer cool flame and most fuel consumed in premixed burn. Both combustion modes burnout similarly. Understanding the predicted sources for the shapes of these curves is the major focus of this paper.

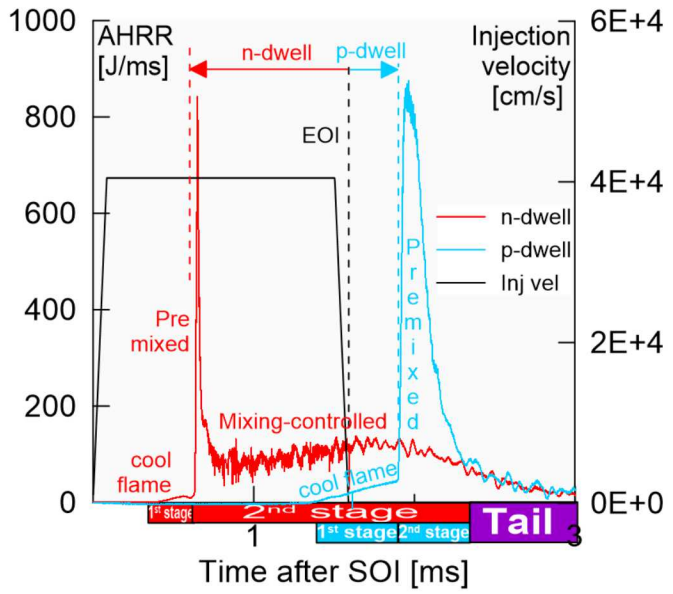

Figure 3. Definition of negative and positive dwell using simulated AHRR curves and injection profile. The figure identifies these cases as 'n-dwell' and 'p-dwell' respectively.

The Results section analyzes the AHRR curves in stages, as noted along the time axis of Figure 3 (SOI stands for start of injection). Cool flame heat release dominates the 1st stage for both cases. Both jets burn premixed during the 2nd stage, however n-dwell transitions quickly to mixing-controlled heat release. Slower mixing characterizes the Tail stage as the burning jets burnout.

Table 1 lists simulation conditions that produced the aforementioned AHRR curves. Ignition dwell was changed by adjusting the chamber gas temperature (Table 1). Pressure was adjusted to maintain chamber density.

Table 1. Simulation conditions.

Number of injector holes	1	
Nozzle diameter	141 µm	
Fuel mass	5.6 mg, n-dodecane ($C_{12}H_{26}$)	
Injection duration	1.5 ms	
Ambient gases composition, O_2 / N_2	21 / 79% by volume	
Initial gas density	18.4 kg/m3	
Case	n-dwell	p-dwell
Initial gas temperature	900 K	760 K
Initial gas pressure	48.5 bar	41.0 bar
Adiabatic		

Results

The purpose of this section is to interpret n-dwell and p-dwell CFD results in terms of their AHRR curves through the use of images and graphs that identify where and how the fuel, during each segment of the curve, is predicted to burn. Note that line graphs represent AHRR and colored renderings represent chemical heat release rate (HRR). At times, "(chemical) HRR" is used in place of "HRR" for emphasis.

n-dwell 1st stage heat release

The simulations are 2D-axisymmetric, so the jet renderings that follow show only a 2D slice of the jet. Before the AHRR curve crosses the AHRR = 0 axis (Figure 4a, 0.38ms), heat release is visible on the jet (Figure 4b, cyan color).

a

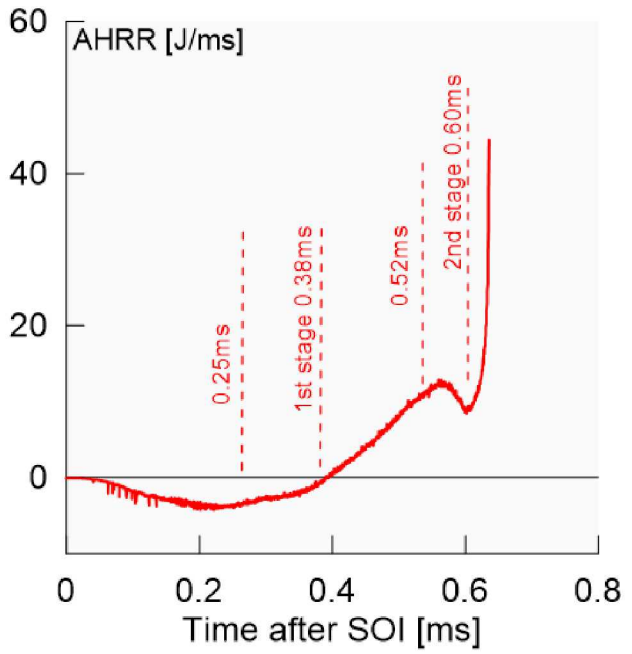

b

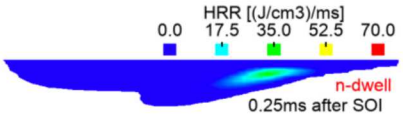

Figure 4. a) n-dwell AHRR curve highlighting segment prior to 2nd stage ignition. b) n-dwell jet colored by (chemical) HRR at 0.25ms after SOI. Jet points right-to-left.

This heat release occurs where hot-ambient gases that surround the jet are entrained into the jet (Figure 5).

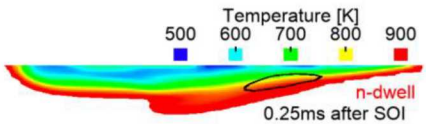

Figure 5. Temperature-colored jet at 0.25ms after SOI. Black outline encompasses heat release location from Figure 4b.

Fuel reaches this heat release zone from inside the jet (Figure 6). Here, equivalence ratio (PHI) is high at the jet axis and leans out radially. PHI >= 0.05 defines the jet outline. The jet size and shape are relatively insensitive near this threshold PHI value and therefore it is selected as a reasonable choice for jet definition.

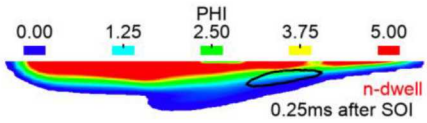

Figure 6. Equivalence ratio-colored jet at 0.25ms after SOI. Black outline encompasses heat release location from Figure 4b. The 'progress equivalence ratio' [31] is used throughout the paper, PHI=(2(#carbon atoms)+0.5*(#hydrogen atoms))/(#oxygen atoms), not including contributions from CO2 and H2O..*

The third requirement for heat release is time, hence heat release is observed some distance downstream from the nozzle where the fuel-rich cool and fuel-lean hot gases have had sufficient time to mix.

Besides sub-grid molecular and turbulent diffusion contributions to mixing, large-scale flow velocity oscillations near the jet centerline, predicted to form very near the injector nozzle and progress downstream for the duration of injection, are also believed to enhance mixing [32]. In Figure 7, blue indicates flow toward the axis and red, away. Alternating colors signify oscillations, which start out very small near the nozzle and grow in size downstream. At this time, two outward-flowing (red) oscillations contact the heat release region, transporting fuel-rich gas there.

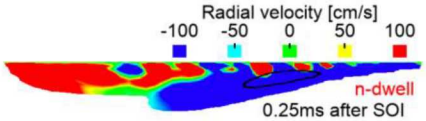

Figure 7. Radial velocity-colored jet at 0.25ms after SOI. Black outline encompasses heat release location from Figure 4b.

A reason that heat release appears visually on the jet (Figure 4b) prior to the AHRR curve becoming positive is because evaporative cooling in some parts of the jet offset the pocket of positive heat release in Figure 4b. At the point where the heat release rate balances the evaporative cooling rate, the AHRR curve crosses the AHRR = 0 axis.

Figure 8 is a close approximation to the time when the evaporative cooling rate and HRR balance. The area under the HRR surface, HRR being as a positive quantity, and the area above the evaporative cooling rate surface, treated as negative, are approximately equal. White lines are added to the HRR surface and black lines to the evaporation rate surface simply to highlight their shapes. The left rendering alone could give the impression that the total evaporation rate is much higher, because its magnitudes are large, but the right rendering shows how narrow the evaporation rate surface is. It is interesting to see how concentrated evaporation is along the jet axis. Simulating with the assumption of axi-symmetry could be

contributing to the large magnitudes, since the flow oscillations seen in Figure 7 could be 3-dimensional in an actual jet.

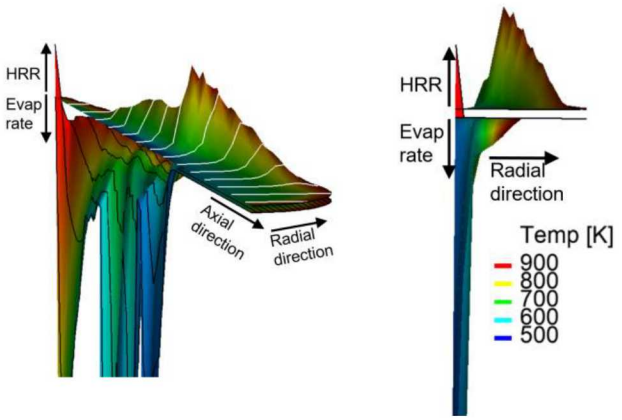

Figure 8. n-dwell: Two views of temperature-colored elevated surfaces when AHRR~0. Top surface) HRR, bottom) evaporation rate. Units: (J/cm^3)/ms. White and black lines highlight surface shapes. Left rendering) Angled view, spray points slightly downward and out of the paper.. Right rendering) nozzle directed directly out of the page. Gap imposed between surfaces for clarity. Compare to 0.38ms location on line graph of Figure 4a.

Gases get colder downstream up until evaporation is complete (Figure 8, left rendering, surface color changes red-to-blue). The right rendering shows the radial relationship between evaporation and heat release, as the lower surface nearly morphs into the upper. From these renderings it is understood why the *early stages of n-dwell heat release* are located offset from the spray axis and do not penetrate all the way to the axis, at least until the point where all fuel is evaporated is passed.

Figure 9 highlights this prediction. The HR zone travels downstream offset from the axis (Figure 9a-b). By 0.52ms after SOI, the HR zone approaches the spray axis farther downstream (Figure 9c). High temperature from two sources accompany the zone. The first is heat release itself (compare Figure 9c and Figure 9d, downstream, HRR and temperature contours match). The second source is upstream where hot-ambient gas is entrained (compare Figure 9d and Figure 9e, blue in Figure 9e means flow is toward the axis). Therefore, beyond the point of complete evaporation (Figure 9f, downstream tip of blue region), the relatively cold near-axis gases can only heat up from the high-temperature sources, as the source of cooling, i.e., evaporation, is exhausted. It is interesting that even while heat release is sweeping through the jet's head (Figure 9c), consuming fuel and presumably creating radical species, through a combination of incomplete combustion and possibly replenishing of fuel vapor from upstream, the equivalence ratio remains high there (Figure 9g). Figure 9 represents n-dwell 1st stage, cool-flame processes noted on the AHRR line graphs of Figure 3 and Figure 4.

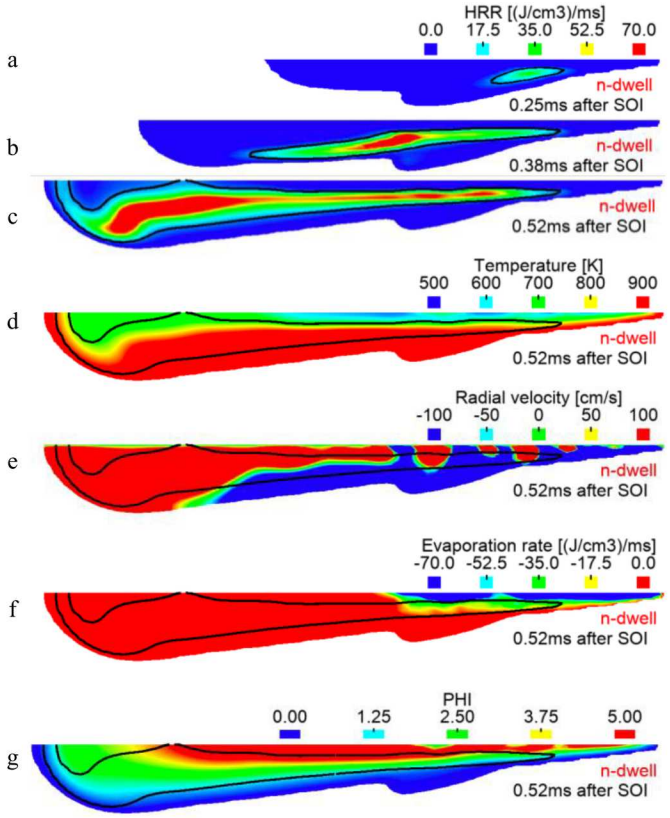

Figure 9. a-c) HRR-colored jet from early HR stages to peak of 1st stage AHRR curve (compare to line graph of Figure 4a). c-g) HRR, Temperature, Radial velocity, Evaporation rate and equivalence ratio-colored jet at peak of 1st stage heat release. Times are after SOI.

Considering just one radical species, formaldehyde, a species commonly measured during 1st stage ignition, initially its concentration is relatively high upstream, then later it is high throughout a majority of the mid- and downstream jet, even touching the spray axis (Figure 10a-b). Formaldehyde is predicted to *form* steadily along the same trajectory as the HR, with little to no formation at the axis (Figure 10c-d, black curve outlines high-HR region). Animations between 0.38 and 0.52ms show formaldehyde to convect steadily inward from where it forms, thus 'filling' the mid- to downstream jet.

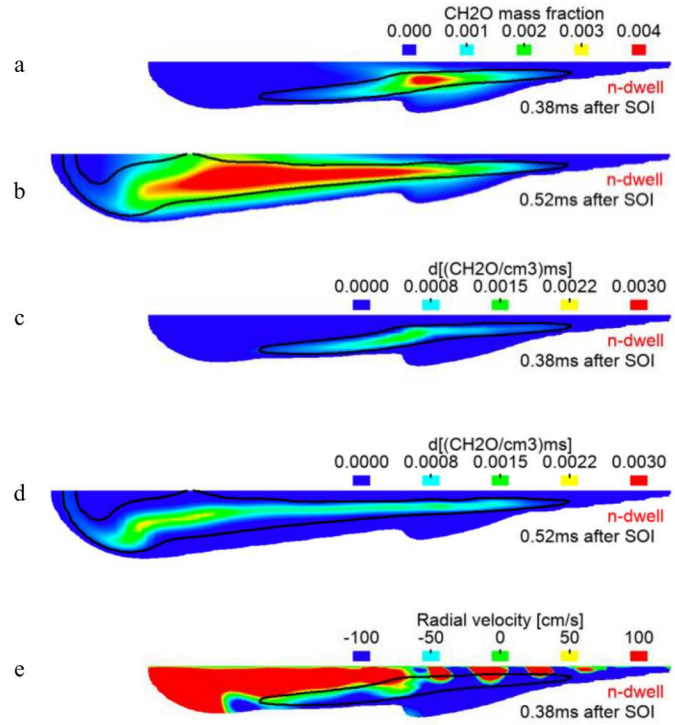

Figure 10. a-b) CH2O mass fraction-colored jet. c-d) CH2O formation-rated-colored jet. e) Radial velocity-colored jet, blue is toward the axis and red is away. Black curve: HR outline. Times are after SOI.

Notice that upstream, formaldehyde forms in an entrained-flow regime (compare Figure 10c-d to Figure 10e (blue is flow toward axis)), which facilitates visualization of the observed result. This suggests that formaldehyde can be used as an indicator of early-stage heat release, but that its observed location might not always be where it forms, and therefore it may not always be representative of the heat release location. Also, where HR does not readily penetrate into the inner jet due to the cold temperatures there, the cold temperatures appear to delay formaldehyde consumption and it accumulates in the jet.

At 0.52ms after SOI, the HR zone approaches the jet's head, which contains an ignitable gas mixture at temperatures supportive of cool-flame heat release (Figure 9c, Figure 9g, Figure 9d respectively). Comparing the high HR (red) region of Figure 9c to its location in Figure 11a, cool-flame heat release propagated through this mixture and this stage of ignition completes. During this time there is a slight decrease in the AHRR curve (Figure 4a, just beyond 0.52ms after SOI). The AHRR decrease is due, in part, to the jet's size as opposed to negative temperature coefficient (NTC) reactions, because (chemical) HRR is only positive in the jet at this time (Figure 11b, elevated HRR surface, upward elevation is positive). It will be demonstrated in the p-dwell section that when the jet is larger, unreacted premixed gases are still present and reacting in the head of the jet when the partially-reacted premixed gases begin their 2nd-stage HR and in that case, no similar dip in the AHRR curve is observed.

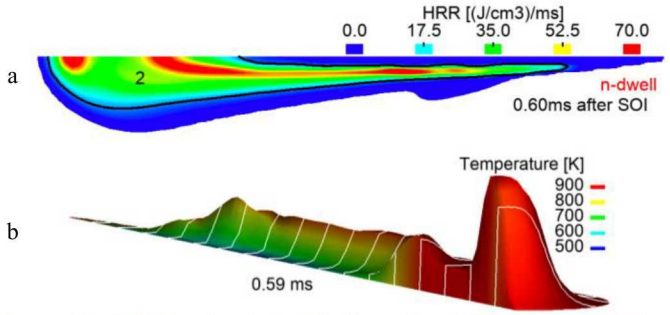

Figure 11. a) HRR-colored jet at 0.60ms after SOI (just prior to 2nd stage ignition). Downstream-most HR zone of Figure 9c (0.52ms after SOI) propagates through mixture at head reaching the jet tip in this figure. Number 2 identifies upcoming-emergence of 2nd stage ignition zone. b) Temperature-colored HR elevated surface pointing left-to-right; upward elevation is positive HRR. White lines accent surface shape.

As 1st stage ignition ends, 2nd stage begins (Figure 4a and Figure 11a, yellow region marked with number '2'). A large number of species exist on the jet at this time. The OH distribution correlates closely with the HR distribution of Figure 11a and is a good indicator of the 2nd stage ignition location (Figure 12).

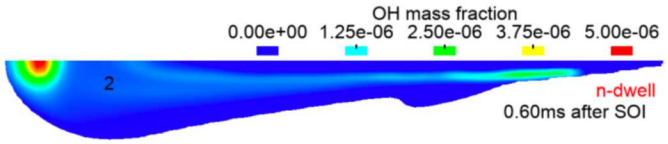

Figure 12. OH-colored jet just prior to 2nd stage ignition. Also see Figure 11a for comparison to HRR. Number 2 identifies upcoming-emergence of 2nd stage ignition location.

n-dwell 2nd stage heat release – premixed burn

2nd stage ignition occurs partway through injection (Figure 3). Higher rates of heat release propagate outward from the downstream hot-concentration of OH (Figure 13a-c, figures use larger HRR and temperature ranges to reflect magnitude increases and the jet size is rescaled with respect to earlier figures), where temperature is high and the mixture is ignitable (Figure 13d). That distribution's shape appears governed mainly by transport via the axial-velocity established within the jet (Figure 13e, compare axial-velocity contours to contours of other scalars).

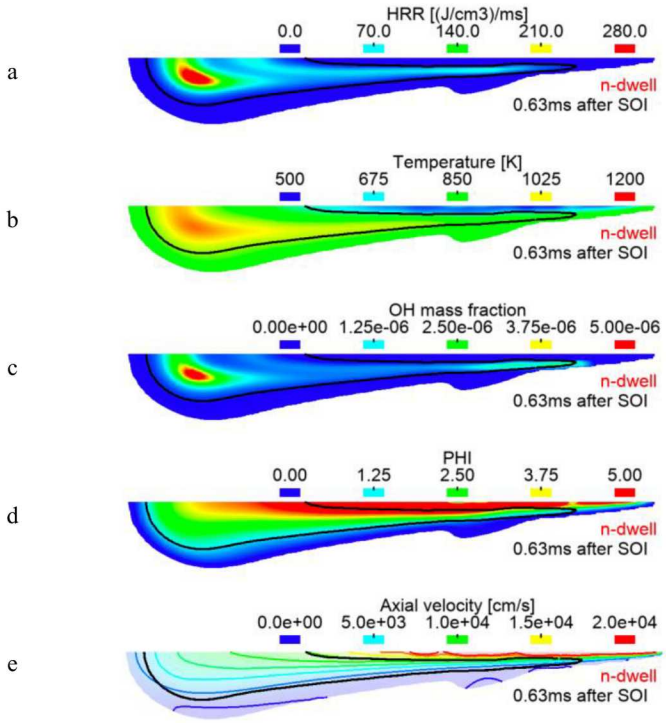

Figure 13. Distributions within the jet at the start of 2nd stage ignition. a) HRR, b) Temperature, c) OH, d) PHI, e) Axial velocity. HRR and temperature color-legends reflect magnitude increases with respect to earlier figures. Jet size is rescaled with respect to earlier figures to facilitate analysis. d-e) Black outline locates high-HR region. Times are after SOI.

By 0.65ms after SOI, the downstream heat release has spread to the radial extent of the jet (Figure 14a), beyond which there are insufficient reactants to propagate heat release farther (Figure 14b). Upstream-to-midstream heat release are bridged along a path of ignitable gas that bounds the still-cool jet core (Figure 14a-c, figures include black outline of the high-HR region). Shown later, the downstream flame propagates up along this bridge until settling at the lift-off-length.

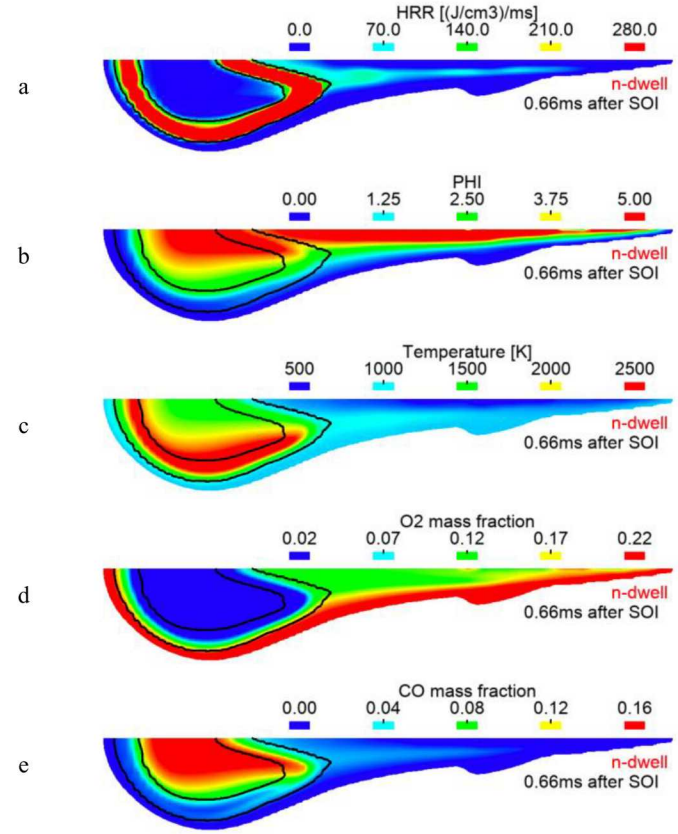

Figure 14. At 0.66ms after SOI (into 2nd stage heat release) the jet colored by: a) HRR, b) PHI, c) Temperature, d) O2 mass fraction, e) CO mass fraction. Black outline bounds the high HR zone. Times are after SOI.

The HR structure at the head bounds an inner core of gas that is not burning (Figure 14a), because there is little oxygen there (Figure 14d). Partially-reacted fuel, in the form of CO, is the dominant reactant within this core (Figure 14e), reaching mass fraction values of 0.16. N_2 is the dominant non-reactive species and water concentration reached 0.10 there.

The burning mode varies around the inner-core circumference. Gases enter this zone along the spray axis at relatively cool flame temperatures (Figure 14c) with sufficient oxygen to burn (Figure 14d). There, post-reaction temperatures reach ~1500K, which is sufficient to form CO (Figure 14e), but insufficient for complete combustion; nearly all oxygen is already consumed.

As an aside, pay close attention to the black-colored HR outline in this and coming figures. The outline is a HR contour that bounds a portion of the HR zone. For example, its value in Figure 14 is 100 [(J/cm^3)/ms], which bounds the red portion of the HR zone *on both sides*. Viewing the jet's colored-scalar with respect to the HR outline shows how the scalar value changes when traversing the HR zone. CO concentration, for example, increases when entering the zone along the axis (Figure 14e, blue-to-red), then decreases when leaving the zone radially and downstream (red-to-blue).

Gases leaving the high-HR zone radially and downstream burn differently than those entering along the axis. Radially and

downstream, CO is the fuel entering the high-HR zone. Oxygen from outside the jet is of sufficient concentration for reaction, and temperatures are sufficient to carry the CO-dominant gases to complete combustion (CO concentration goes blue, meaning it approaches zero).

Next, the HRR color-legend is rescaled to bring out a third burn mode located around the HR zone upstream tip (Figure 15a-b at 0.63 and 0.66ms). Increasing the maximum HRR color-legend value from 280 to 1200 [(J/cm3)/ms] (compare Figure 14a to Figure 15b) highlights higher HRR at the tip more than along the side or downstream ends of the HR zone, suggesting that more than CO reactions take place there. At 0.63ms after SOI hydrogen-peroxide exists throughout most of the jet (Figure 15c, black indicates the high-HR region at that time). Hydrogen-peroxide decomposition is known to lead to rapid heat release. Decomposition is observed in Figure 15d at 0.66ms across the HR-zone tip, thus an additional contribution to HR is identified. The results suggest that the HR-zone expansion at the tip is more than due to propagation; it is also aided by advection with the velocity vectors having an upstream component that disrupts the oncoming flow (Figure 15e). The disruption diverts oncoming gases toward the HR-zone outer side (Figure 15d, arrow) adding to the HRR there (Figure 15b). The disruption also decreases the near-axis crossflow area, which accelerates flow velocity there. However, this transient was not investigated in detail for this study.

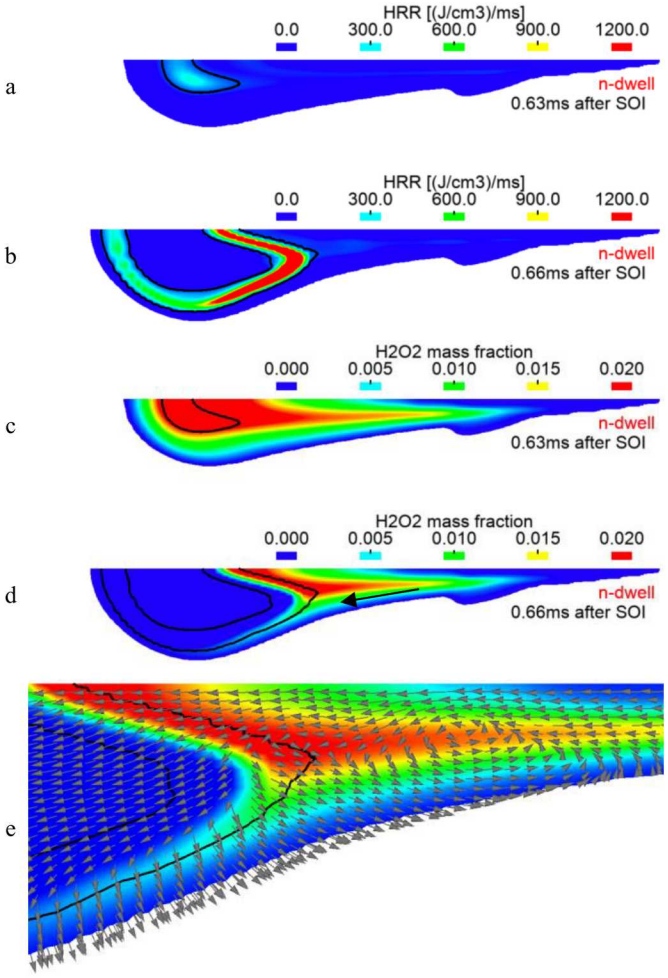

Figure 15. At 0.63 and 0.66ms after SOI, the jet colored by: a-b) HRR, c-e) Hydrogen-peroxide mass fraction, including the HR zone outline (black); e) includes velocity vectors (gray). Times are after SOI.

The processes just described are predicted to occur during n-dwell simulated premixed burn (Figure 16).

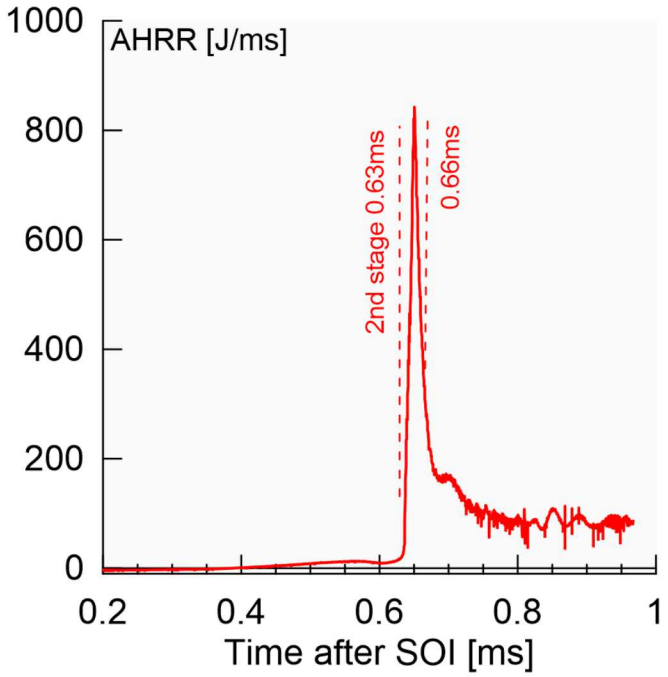

Figure 16. n-dwell AHRR vs. time after SOI highlighting premixed burn portion of 2nd stage heat release.

n-dwell 2nd stage heat release – mixing-controlled burn

Beyond 0.65ms after the SOI, the premixed burn continues its transition to a mixing-controlled burn, which coincides with progression of the HR tip moving farther upstream until a steady lift-off length, LOL, is established. At 0.70ms after SOI there is an interesting transition in flame structure; the radially-outward flame splits with both branches anchored at the upstream tip (Figure 17a). Using the upstream tip as a reference location, heat release progresses downstream along rich, stoichiometric and lean branches (Figure 17b).

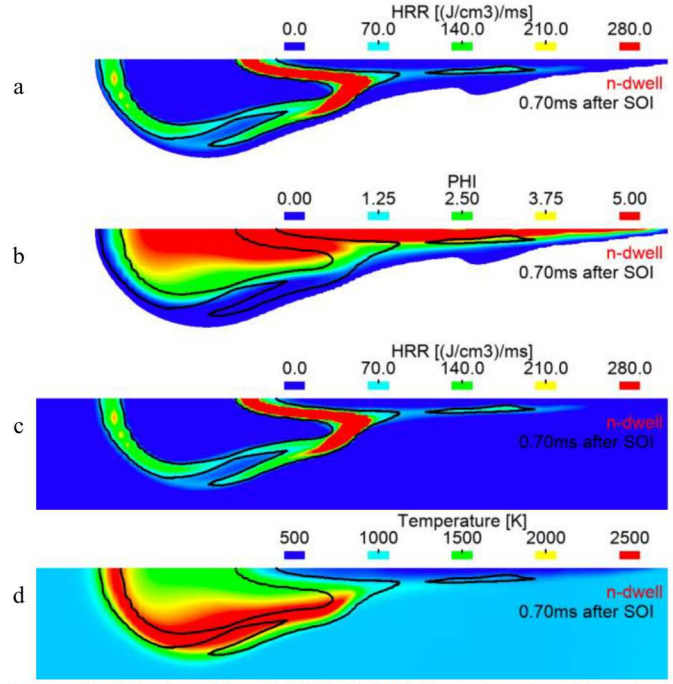

Figure 17. Jet colored by: a) HRR, b) PHI. Domain colored by: c) HRR, d) Temperature. Includes black HR outline. Times are after SOI.

Removing references to the jet for a moment and considering the HR structure alone (Figure 17c), the branches can be interpreted as heat release progressing downstream at rates determined by the local turbulent flame speed (Figure 17b, in terms of equivalence ratio). This perspective is quite different from that of Figure 14 and Figure 15. Processes associated with those figures relate heat release in terms of jet development. On the other hand, heat release upstream of the HR tip of Figure 17c can be thought of as an ignition source. Animations suggest that once beyond the confines of the evaporation-cooled gases (Figure 17d), *flames* appear to progress downstream *from there*, i.e., from the HR-upstream tip, at rates determined by the local flame speed. Although further analysis is needed to confirm this interpretation, in this perspective, mixing governs the equivalence ratio distribution along the stoichiometric branch, but heat release itself stems from the HR tip and propagates along the length of the boundary as reactive species along the boundary are replenished from the jet on one side and from the ambient on the other. It might turn out to be reasonable to assume that heat release along these branches is a combination of both processes, local reactions due to at-boundary mixing and due to up- to downstream flame propagation along the branches.

At 0.87ms after SOI the lean-HR branch is minimal in length and the jet is quasi-steady (Figure 18a). Intermediate species that earlier collected downstream (Figure 15c-d) have been consumed (Figure 18b) as the flame settles upstream at the LOL. The temperature distribution changed little from its pre-quasi-steady form (compare Figure 14c to Figure 18c) and downstream is still heavy with CO and light on O2 (Figure 18d-e). It is worth noting that, should near-axis cool-flame heat release occur at experimental conditions, it might be difficult to detect if it is surrounded by hotter, OH-producing flames (Figure 18a,f).

At this time, the far-upstream heat release feeds the LOL location (Figure 18a) and consumes oxygen along the way (Figure 18e). The simulated jet's oscillatory nature periodically transports oxygen-depleted gas radially inward (Figure 18h, blue is inward, red is outward) such that burning along the flame/evaporation zone border is rich (Figure 18g) limiting the extent of combustion there, limiting it apparently to producing mainly CO (Figure 18d).

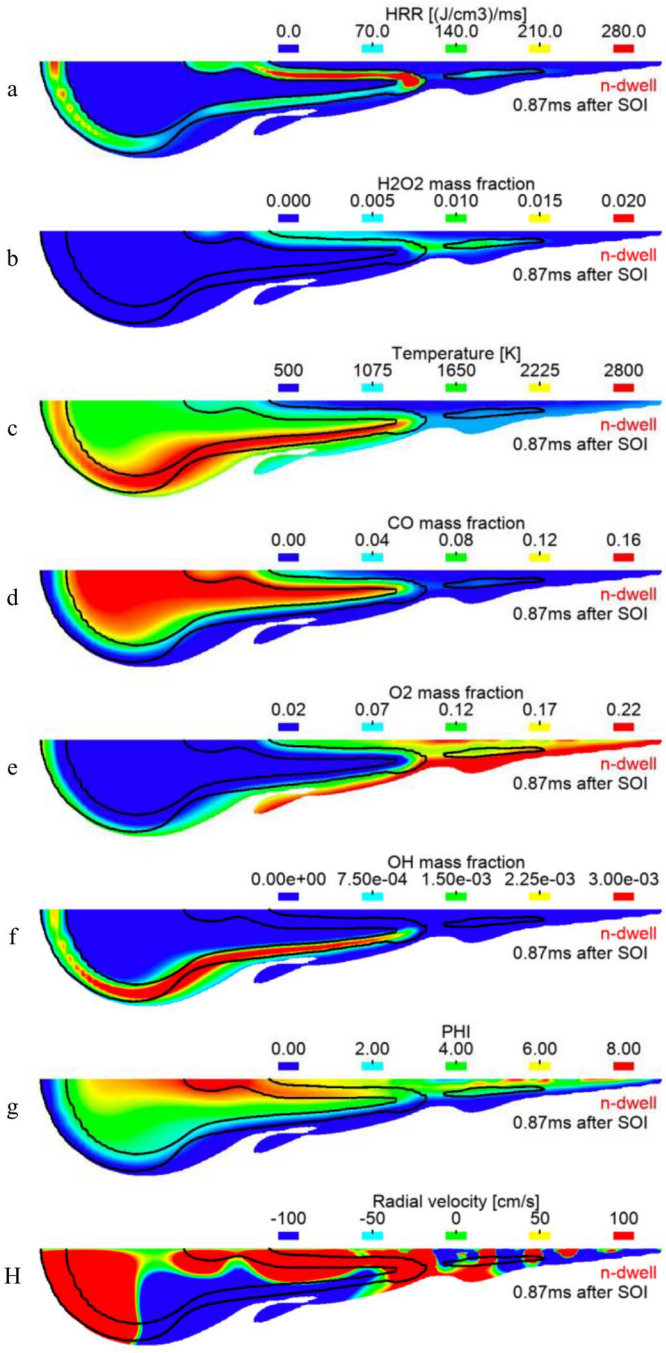

Figure 18. Jet colored by: a) HRR, b) H_2O_2 mass fraction, c) Temperature, d-f) CO, O_2, OH mass fractions, g) equivalence ratio, h) radial velocity. Note that scalar values can and often times do extend below and above the legend ranges and sometimes by a large amount. HRR and radial velocity are two examples. Selected ranges highlight features of interest. Times are after SOI.

The jet exhibits the just mentioned behaviors from approximately 0.78 to 1.70ms after SOI (Figure 19). Keep in mind that the jet is transient and the figures represent a single instant in time. Characteristics that vary over this timeframe are flow oscillations originating near the nozzle that travel upstream, and pulses of evaporation and heat release that do similar, causing the rich HR branch to waver substantially changing its downstream reach, while the jet's head continues penetrating with near-axis heat release expanding the jet radially. Animations show that the heat release at the jet head along the jet axis (Figure 18a, red HRR far downstream) propagates along the high-HR zone periphery, first radially outward, then upstream, in a manner similar to that mentioned for HR propagating downstream from the LOL along the stoichiometric branch. Heat release propagation from each end of the stoichiometric branch could explain why the HRR decreases midway between the LOL and near-axis jet head (Figure 18a). Low-HR locations about the jet periphery could allow soot to escape the jet, making it difficult to oxidize later in the cycle. This warrants further analysis.

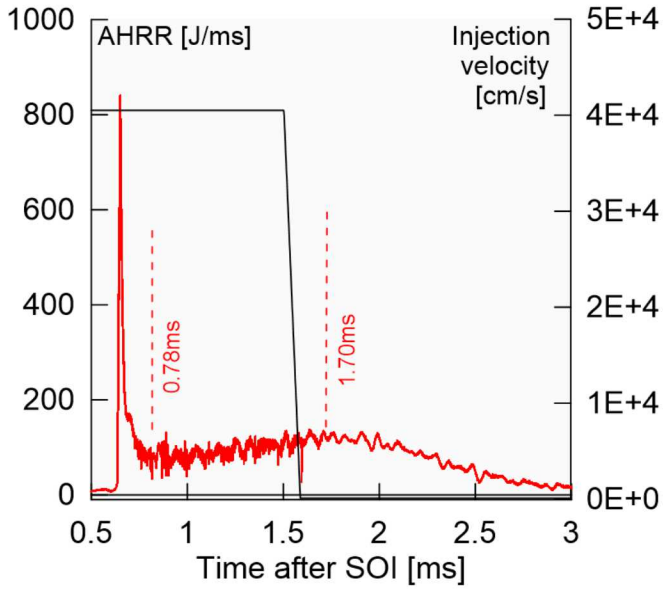

Figure 19. AHRR vs. time after SOI highlighting n-dwell mixing-controlled burn.

After the EOI, the jet divides at the LOL (Figure 20a). Heat release continues at the LOL while upstream fuel continues flowing downstream and similar observation holds at the jet's downstream-most tip (cyan regions of Figure 20a). Upstream burns cold, while downstream-CO burns hot (Figure 20b-c) from outside of the jet, and inward (burning represented by OH, Figure 20d). Outside of the jet is where the oxygen is (Figure 20e), although in low concentration at the jet boundary (Figure 20e, white outline). These processes occur after 1.70ms (Figure 19) with both burn zones shrinking in size until they are exhausted.

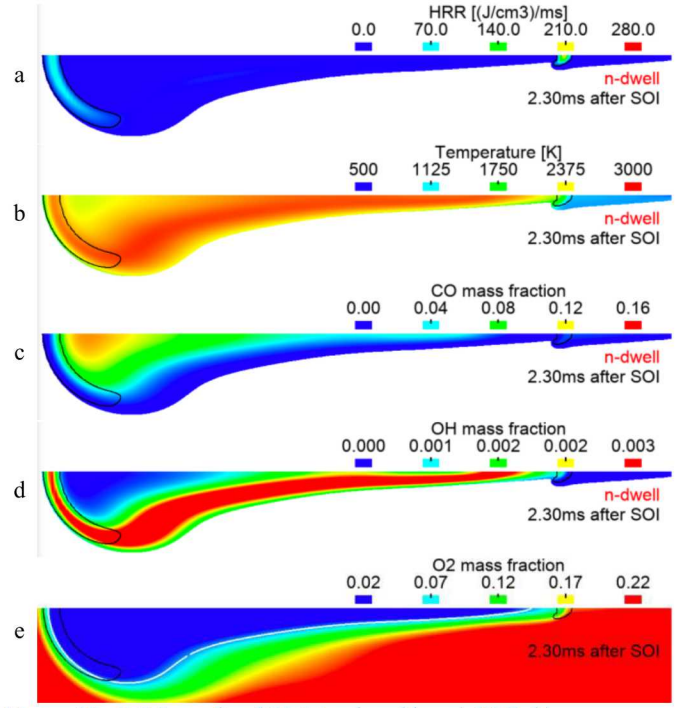

Figure 20. At 2.3ms after SOI, jet colored by: a) HRR, b) Temperature, c-d) CO, OH mass fraction. e) Domain colored by O2 mass fraction with jet outline (white curve). Renderings are representative of time following 1.70ms after SOI (see AHRR curve, Figure 19). Times are after SOI.

p-dwell 1st stage heat release

The p-dwell case AHRR curve becomes positive at about 1.33ms after SOI, when n-dwell is midway through its mixing-controlled burn (Figure 21).

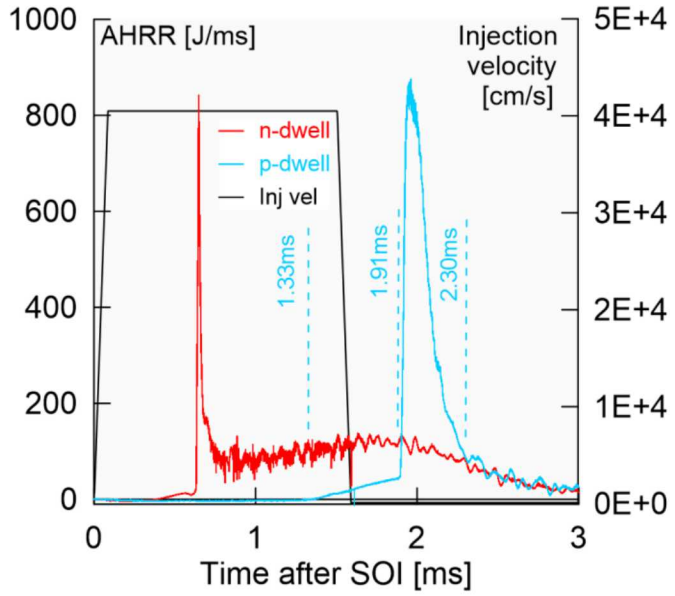

Figure 21. n-dwell and p-dwell AHRR and their common injection profile. p-dwell start of 1st and 2nd stage ignition, 1.33, 1.91ms. Start of AHRR tail, 2.30ms.

At this time:

- The p-dwell peak (chemical) HRR is only 1/3 of the n-dwell peak value when its curve crossed AHRR = 0 (compare Figure 22 to Figure 8).
- Like n-dwell, p-dwell evaporation is concentrated at the axis and HR is offset radially (compare the same figures).
- All p-dwell gases are relatively cool (no yellow-to-red).

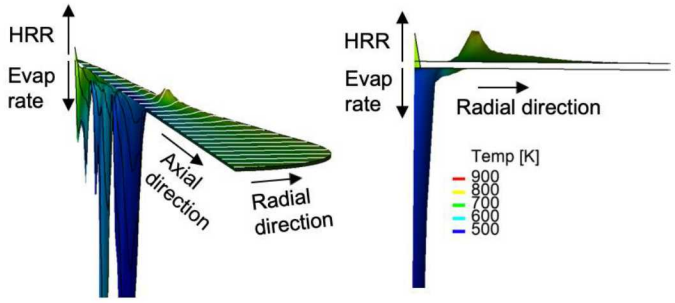

Figure 22. p-dwell: Two views of temperature-colored elevated surfaces when AHRR=0. Top surface) HRR, bottom) evaporation rate. Units: (J/cm³)/ms. White and black lines highlight surface shapes. Left rendering) Nozzle is pointed left-to-right. Right rendering) nozzle directed out of the page. Gap imposed between surfaces for clarity.

Figure 23 compares both cases at their respective start of 1st stage ignition timings. It is seen that the peak HRR values and their placement upstream differ. Similar evaporation and temperature distributions locate the initial heat release offset from the spray axis

(Figure 23b-c, see the n-dwell section for a discussion of initial radially offset heat release).

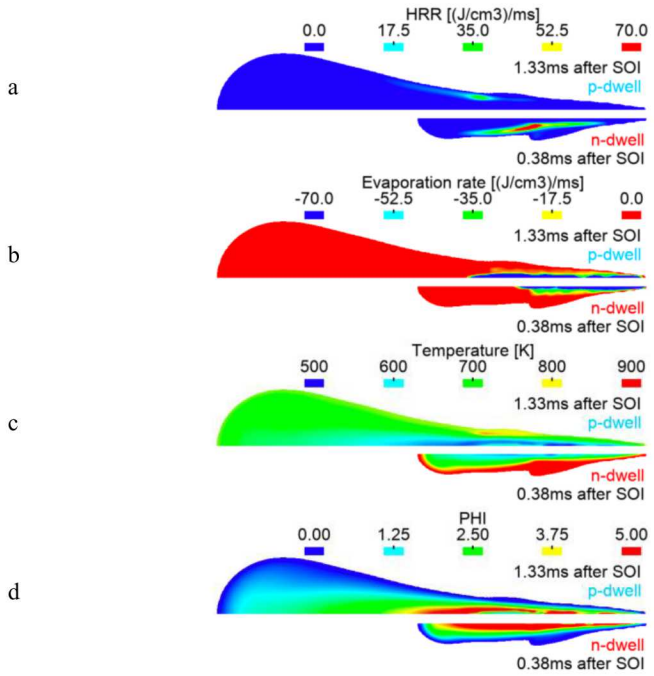

Figure 23. Compares cases at their respective start of 1st stage ignition. a) HRR, b) Evaporation rate, c) Temperature, d) equivalence ratio. Color legends apply to both cases and relative size scaling is accurate. Times are after SOI.

The jet-size differences are obvious. By the 1st stage ignition timing, p-dwell has evaporated 4.4 times more fuel in the jet and this difference is apparent from the equivalence ratio distribution renderings (Figure 23d, p-dwell 4.8, n-dwell 1.1mg evaporated); the p-dwell jet has a larger volume of premixed charge. Note that fuel located at the head extends farther radially and therefore occupies a much larger volume than near-nozzle fuel, so even relatively low equivalence ratio values there may represent a non-negligible fuel mass.

The p-dwell duration of 1st stage heat release is relatively long (Figure 21, p-dwell 0.58ms, n-dwell 0.22ms) and during that extended time, more heat is released (p-dwell 18J, n-dwell 4J). As described next, Figure 24 locates this heat release on the jet.

As seen previously, n-dwell 1st stage heat release initiates mid-stream at the jet-radial extent, then sweeps through to the jet's tip (Figure 24a, snippets from earlier figures). When the heat release reaches the spray axis (Figure 24a, 0.57 and 0.59ms), the flame appears to split. Upstream and on-axis, the jet actively replenishes reactants and the HRR remains high there. Downstream still contains unburned-premixed charge, so the HRR remains high there as well. Radially the mixture is oxygen depleted for two reasons. In a static sense, those gases have already burned at this thermochemical state. In a dynamic sense, the aforementioned reaction zone consumes entrained oxygen brought forward by the jet. Therefore, reactions in the radial direction are slower and the flame appears to split (Figure 24a, 0.59ms and Figure 4, dip in AHRR curve).

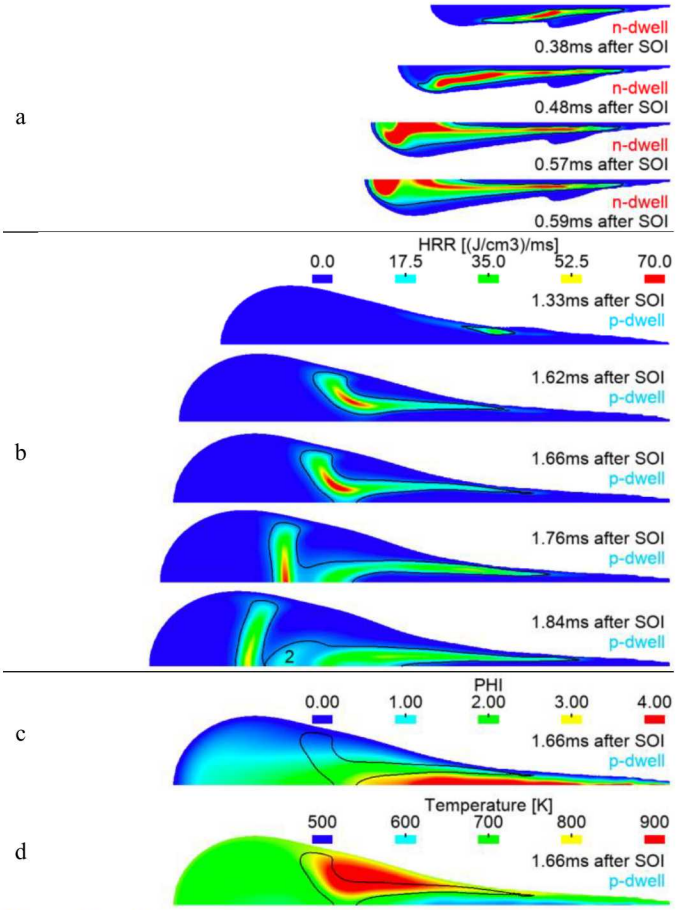

Figure 24. a) Summary of n-dwell, 1st stage HRR. Relate renderings to AHRR curve (Figure 4a). b) p-dwell 1st stage HRR progression. Relate renderings to AHRR curve (Figure 21). Number 2 locates origin of 2nd stage ignition. c-d) p-dwell equivalence ratio and temperature @1.66ms with high-HR zone outline (black curve). Times are after SOI.

The p-dwell 1st stage heat release is predicted to be similar in nature, but with notable exceptions. Namely, the heat release reaches the axis farther downstream (Figure 24b 1.66ms), still facing a large volume of lean-premixed charge ahead and a smaller volume of rich-premixed charge behind it (Figure 24c).

The 1st stage heat release temperature distribution is also quite different on the jets. The p-dwell jet periphery is at or above 900K only where reactions take place (Figure 24d), while the n-dwell jet periphery is at those temperatures all along (Figure 9d). With fuel injection over and with reaction rates slower between the flame fronts, each front propagates in opposite-axial directions and between-flame gases lead to 2nd stage ignition (Figure 24b, 1.76 and 1.84ms).

Like the n-dwell case, the p-dwell formaldehyde concentration does not appear to be an exact indicator of the 1st stage HR location (Figure 25a, black line is high-HR outline and time is near the end of 1st stage heat release). Unlike n-dwell, p-dwell formaldehyde shows where the HR has already occurred, rather than where it has been transported by the jet; this could be because injection is over, and therefore p-dwell jet velocities are slower at this time. Near the end

of 1st stage heat release, hydrogen-peroxide is surrounded in all outward directions by hot reactants and therefore fast reaction rates are anticipated (Figure 25b-e).

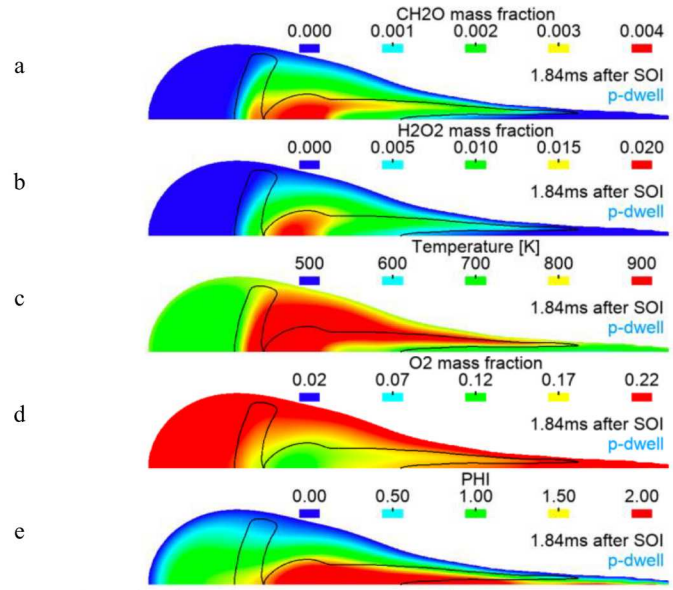

Figure 25. p-dwell jet characteristics near end of 1st stage heat release. a,b,d) CH2O, H2O2, O2 mass fractions, c) Temperature, e) equivalence ratio. Black curve outlines high-HR zones. Times are after SOI.

p-dwell 2nd stage heat release

The premixed burn portion of n-dwell 2nd stage heat release propagated through the jet relatively quickly, in 0.05ms (Figure 16 (AHRR line graph) and Figure 26a-b).

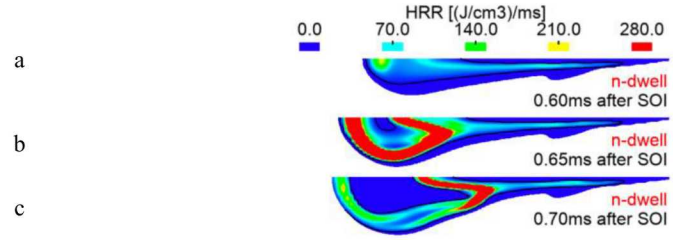

Figure 26. n-dwell: a,b) HR propagation through jet's head during 2nd stage premixed burn. c) Transition from premixed to mixing-controlled burn. Same size and color scaling as Figure 27.

The p-dwell 2nd stage heat release is mainly a premixed burn, which lasts nearly 8 times longer, 0.39ms (Figure 21 (AHRR line graph) and Figure 27a-f). Take note of the predicted similarities in the n-dwell and p-dwell premixed burn structures. Both are predicted to start downstream, on axis and between two hotter flames, then propagate outward in all directions (Figure 26a-b and Figure 27a-c). With time, regions of the p-dwell jet exhaust local reactants and the jet, as defined, burns out downstream (Figure 27e-f, white regions). Even this process has structural similarities to the n-dwell case when it is in transition from premixed to a mixing-controlled burn (compare to Figure 26c). However, downstream n-dwell jet burnout following premixed heat release does not occur, because injection is ongoing, replenishing reactants.

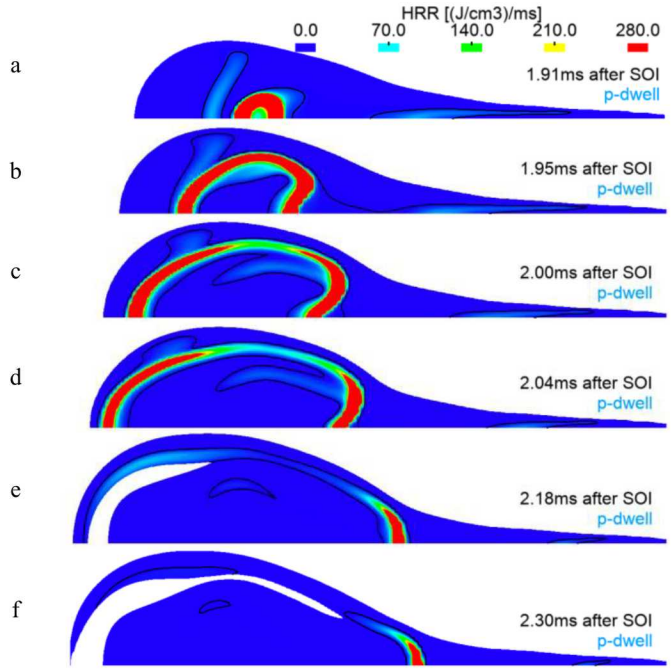

Figure 27. p-dwell premixed HR progression through jet. Compare to Figure 26a-b, which has the same size and color scaling. Times are after SOI.

By the time of p-dwell peak HRR, 2nd stage reactions have propagated midway through the jet and 1st and 2nd stage HR zones are merged; there, temperatures are high, as are high-temperature reaction rates (Figure 28a-c, numbers 1 and 2 indicate 1st and 2nd stage high-HR zones). With high concentrations of formaldehyde and hydrogen-peroxide, upstream reactions are akin to 1st stage heat release (Figure 28d-e). The lower near-axis upstream oxygen concentration is the likely cause (Figure 28f).

Oxygen is consumed within the flame envelope, but reactions are not complete, keeping equivalence ratios rich (Figure 28f-g). The CO concentration represents equivalence ratio variation within the reaction zone very well (Figure 28h).

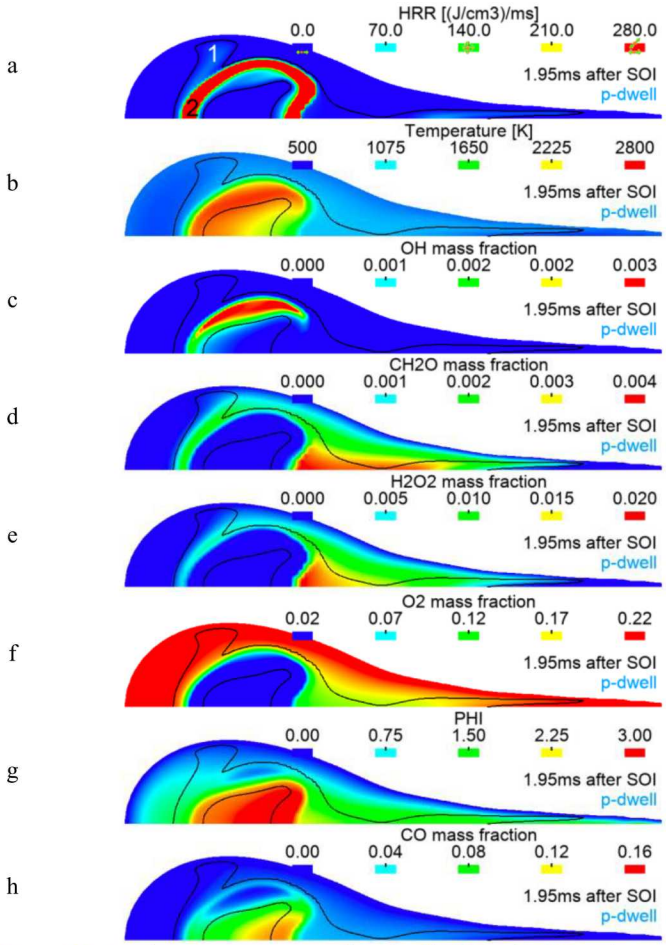

Figure 28. Jet characteristics at peak p-dwell HRR. a) HRR with numbers 1 and 2 indicating 1st and 2nd stage high-HR zones, b) Temperature, c-f) OH, CH_2O, H_2O_2, O_2 mass fraction, g) equivalence ratio, h) CO mass fraction. Times are after SOI.

n-dwell and p-dwell AHRR tail

Figure 28 and Figure 29 renderings are in the same order for ease of comparison. Figure 29 includes both the p-dwell and n-dwell renderings, because beyond this time, globally, they burn similarly (Figure 21), so it is interesting to see how they compare locally.

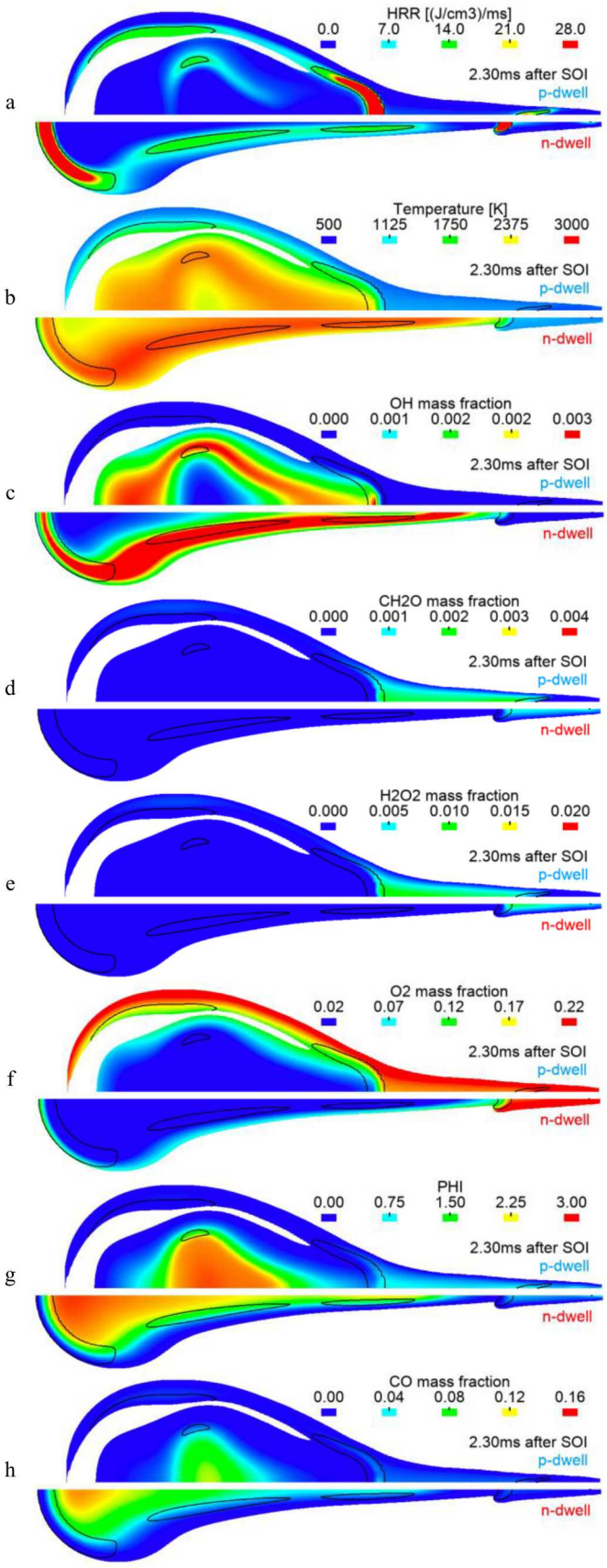
a
HRR [(J/cm3)/ms]
0.0 7.0 14.0 21.0 28.0
2.30ms after SOI
p-dwell
n-dwell
b
Temperature [K]
500 1125 1750 2375 3000
2.30ms after SOI
p-dwell
n-dwell
c
OH mass fraction
0.000 0.001 0.002 0.002 0.003
2.30ms after SOI
p-dwell
n-dwell
d
CH2O mass fraction
0.000 0.001 0.002 0.003 0.004
2.30ms after SOI
p-dwell
n-dwell
e
H2O2 mass fraction
0.000 0.005 0.010 0.015 0.020
2.30ms after SOI
p-dwell
n-dwell
f
O2 mass fraction
0.02 0.07 0.12 0.17 0.22
2.30ms after SOI
p-dwell
n-dwell
g
PHI
0.00 0.75 1.50 2.25 3.00
2.30ms after SOI
p-dwell
n-dwell
h
CO mass fraction
0.00 0.04 0.08 0.12 0.16
2.30ms after SOI
p-dwell
n-dwell

Figure 29. n-dwell and p-dwell jet characteristics at start of AHRR tail. a) HRR, b) Temperature, c-f) OH, CH_2O, H_2O_2, O_2 mass fraction, g) equivalence ratio, h) CO mass fraction. By this time, n-dwell has released 13% more heat than p-dwell (222 vs. 197J). Times are after SOI.

Recall, each case uses the same injection profile, yet the resulting jets differ in shape and size (n-dwell 5.7cm^3, p-dwell 12.6cm^3 at 2.30ms). Within the black outline is where faster reactions occur (Figure 29a). There, the n-dwell case burns closer to stoichiometric and the p-dwell case is very lean (volume-average equivalence ratio within black outline of Figure 29g: n-dwell 0.73, p-dwell 0.12). Note that n-dwell consistently burns on a smaller jet (refer back to start of 1st stage ignition, Figure 23) and by that observation alone, injection schedules being equal, the n-dwell jet is on average, consistently richer.

To be consistent with other figures, Figure 29 renders scalars on the PHI-defined jet. However, to understand HR similarities at and beyond 2.30ms, first consider only regions where high-temperature reactions take place, as represented by the OH concentration (Figure 29c, cyan-to-red). Over this region, temperature distributions and reactant distributions are quite similar case-to-case, with the n-dwell distributions being more elongated (Figure 29b-h). Thus, the local distributions correlate well with their similar global AHRR tails. But, upstream temperature and species distributions differ noticeably between the two cases and these are the gases that will be encountered first by a 2nd injection. For example, a 2nd fuel pulse, injected at 2.3ms after SOI under the conditions of this study, may interact with a relatively hot concentration of OH in the n-dwell case, or with a cool concentration of CH_2O in the p-dwell case. It is difficult to guess how the 1st and 2nd pulses will interact when injected into these different environments based on these images alone, and therefore, experiments and CFD analysis of multiple injections is required.

Summary

Two axisymmetric CFD simulations inject a single pulse of n-dodecane into an air-filled, constant-volume chamber that differs in ambient temperature, namely 900 and 760K. Pressure adjustment is used to maintain the same chamber density to maintain similar entrainment rates into the jets for the two cases. All other case-conditions are also the same. Apparent heat release rate (AHRR) curves are analyzed through visual inspection and quantification of chemical heat release rate (HRR), temperature, equivalence ratio (PHI) and species distributions on the jets. The ignition dwell is negative for the 900K case and positive for the 760K case, therefore, the cases are referred to as n-dwell and p-dwell respectively (e.g., p-dwell reads as 'the positive dwell case'). Motivation for this research is to gain sufficient understanding of the detailed-transient characteristics of diesel jets so that conceptual models of both single and multi-pulse injection schemes can be developed.

For analysis, the AHRR curve is segmented into 1st and 2nd stage heat release and an AHRR tail (Figure 3). The n-dwell case 2nd stage heat release is subdivided into premixed and quasi-steady mixing-controlled burn regions. The simulations predict no quasi-steady mixing-controlled burn for the p-dwell case and therefore it is not subdivided. *Equivalent AHRR-curve segments* are used for analysis and comparison, as opposed to *equal times after SOI*.

Aside from the n-dwell case exhibiting quasi-steady mixing-controlled burn and the p-dwell case not and n-dwell reactions taking place on a steadily growing jet, while the p-dwell jet volume changes little during its heat release, many predicted transient-burn characteristics are really quite similar. Predicted similarities (S:) and differences (D:) include:

- S: Very early heat release begins off-axis because liquid-fuel evaporation keeps near-nozzle, on-axis gases too cool for reactions (Figure 23).
- D: p-dwell early heat release begins later and farther downstream because reaction rates are slower when fuel vapor mixes with cooler ambient gas (also Figure 23).
- S: 1st stage heat release represents consumption of reactants as the reaction zone propagates from the narrow-upstream jet to the wider-downstream jet where a larger quantity of premixed charge is located. Once past the point of complete fuel evaporation, heat release propagates toward the jet axis where the gas mixture is richer (Figure 24).
- D: The p-dwell reaction zone reaches the jet axis farther downstream and later because cool ambient gases extend its evaporation zone farther downstream (Figure 23 and Figure 24).
- S: When the 1st stage reaction zone reaches the jet axis, it can travel no farther radially inward (it is an axisymmetric jet). The reaction zone bifurcates, the upstream branch moving little and the downstream branch propagating toward the jet downstream tip (Figure 24).
- D: n-dwell distance from the bifurcation point to the jet downstream tip is relatively short, its premixed charge is exhausted and as a result, there is a dip in the AHRR curve prior to 2nd stage heat release. p-dwell distance to the jet downstream tip is longer, premixed charge is not exhausted prior to 2nd stage heat release and there is no pre-2nd stage AHRR dip (Figure 24, Figure 3, Figure 4).
- S: Between the bifurcated branches, apparently non-propagating (or slowly propagating) reactions progress and increase local concentrations of intermediate reactive species, (Figure 12, Figure 25b).
- S: Sufficient accumulation of downstream chain-branching species ignites the 2nd stage and reactions propagate once again through the downstream, partially-reacted mixture, this time, outward in all directions (Figure 26a-b, Figure 27a-f).
- D: p-dwell has a larger volume of premixed gases and this burn process continues until the AHRR tail (Figure 27).
- D: n-dwell downstream-premixed gases are consumed quickly. When the premixed-reaction zone reaches the jet periphery, transition from premixed to mixing-controlled burn ensues (Figure 15b, Figure 17a).
- D: The n-dwell reaction zone is reactant-limited radially and downstream, but there is a steady supply of reactants adjacent to the evaporation zone and the reaction zone follows this path upstream; this path is almost identical to the downstream path taken during 1st stage heat release. The process continues until a lift-off length is established (the process is partially represented by Figure 26b-c).
- D: Once quasi-steady, the n-dwell mixing-controlled flame appears to be two flames. One quasi-steady flame is initiated at the lift-off length, fueled by an upstream, partially reacted mixture. One branch of the upstream flame hugs the evaporation zone, the other hugs the jet periphery,

while the other flame appears to initiate at the jet downstream tip, being fueled mainly by CO and propagating upstream along the jet periphery. This is only a possible interpretation that requires more investigation. (Figure 18a,d).

- D: Fuel injection is over at the start of the AHRR tail and at this time, near-nozzle temperature and species distributions differ between the n-dwell and p-dwell cases and vary markedly from the environment seen by the 1st injection pulse (Figure 29).

In the simplest terms, each simulated jet ignites from reactions propagating through it twice. The 1st reaction stage is from upstream to downstream through a premixed, unburned mixture. The 2nd reaction stage follows a similar path, but travels downstream to upstream through a partially-reacted mixture. From its 2nd stage ignition location, the p-dwell case finds ignitable mixture surrounding it in similar quantity in all outward directions and spreads outwardly from there. Conversely, the n-dwell case ignitable mixture is upstream-weighted, which draws its upstream-reaction zone more-heavily toward the nozzle. This detailed understanding of diesel jet ignition and combustion serves as a basis for future studies of multiple injections, expanding on the knowledge acquired by previous work in the multiple-injection area [33,34].

Acknowledgements

This research was performed under Sandia Subcontract 1890589, 1, sponsored by the U.S. Department of Energy (DOE) Office of Energy Efficiency and Renewable Energy (EERE), with program managers Michael Weismiller and Gurpreet Singh. Sandia National Laboratories is a multi-mission laboratory managed and operated by National Technology and Engineering Solutions of Sandia, LLC., a wholly owned subsidiary of Honeywell International, Inc., for the U.S. Department of Energy's National Nuclear Security Administration under contract DE-NA0003525. Images are processed with EnSight visualization software from ANSYS. The granted use of their post-processing software packages is greatly appreciated.

References

1. Andersson Ö, Miles PC, "Diesel and Diesel LTC Combustion" in "Encyclopedia of Automotive Engineering," Crolla D, Foster, DE, Kobayashi T, Vaughan N eds., Hoboken, NJ, John Wiley & Sons, 2014.
2. Hasse C, Peters N, "Modelling of ignition mechanisms and pollutant formation in direct-injection diesel engines with multiple injections," Int. J. Engine Res. 6(3):231–246 (2005).
3. Tomishima H, Matsumoto T, Oki M et al., "The advanced diesel common rail system for achieving a good balance between ecology and economy," SAE Tech. Paper 2008-28-0017, 2008.
4. Ishida M, Chen Z-L, Luo G-F et al., "The effect of pilot injection on combustion in a turbocharged D. I. diesel engine," SAE Tech. Paper 941692, 1994.
5. Kastner O, Atzler F, Rotondi R et al., "Evaluation of Injection Strategies for passenger car diesel engines to meet Euro 6 legislation limits," THIESEL 2008:27–42, Valencia, Spain, 2008.
6. O'Connor J, Musculus MPB, "Post injections for soot reduction in diesel engines: a review of current understanding," SAE Tech. Paper 2013-01-0917, 2013.
7. Hessel RP, Yue Z, Reitz RD, Musculus M, "Advanced CFD Diagnostics: Tracking Soot from Originating Fuel Sources through to EVO in a Cummins N14 Optical Engine Utilizing Post Injections," Panel Presentatoin at SAE 2015 World Congress & Exhibition, Apr. 2015.
8. Reitz RD, Bracco FV, "On the dependence of spray angle and other spray parameters on nozzle design and operating conditions." SAE Technical Paper 790494, 1974.
9. Yue Z, RD Reitz, "An equilibrium phase spray model for high-pressure fuel injection and engine combustion simulations," International Journal of Engine Research, DOI: 10.1177/1468087417744144, 2017.
10. Amsden AA, O'Rourke PJ, Butler TD, "KIVA II: a computer program for chemically reactive flows with sprays." Report no. LA-11560-MS, May 1989. Los Alamos, NM: Los Alamos National Laboratory.
11. Liu A, Mather D, Reitz RD, "Modeling the effects of drop drag and breakup on fuel sprays." SAE Technical Paper 930072, 1993.
12. Abani N, Reitz RD, "Unsteady turbulent round jets and vortex motion," Physics of Fluids 19, 125102 (2007); https://doi.org/10.1063/1.2821910.
13. Hessel, RP, Abani N, Aceves S, Flowers, D, "Gaseous Fuel Injection Modeling Using a Gaseous Sphere Injection Methodology," SAE Technical Paper 2006-01-3265, 2006, https://doi.org/10.4271/2006-01-3265.
14. Ouellette P, "Direct Injection of Natural Gas for Diesel Engine Fueling," Ph. D. Thesis, University of British Columbia, February, 1996.
15. Ouellette, P, Hill PG, "Turbulent Transient Gas Injections," Journal of Fluids Engineering, Volume 122, December 2000, page 743.
16. Perini F, Reitz RD, "Improved atomization, collision and sub-grid scale momentum coupling models for transient vaporizing engine sprays." Int. J. Multiphase Flow. 79, 107–123 (2016).
17. Yoshikawa T, Reitz RD, "Validation of a grid independent spray model and fuel chemistry mechanism for low temperature diesel combustion." Int. J. Spray Combustion 2009; 1(3): 283–316.
18. Abani N, Kokjohn S, Park S, Bergin M, Munnannur A, Ning W, Sun Y, Reitz RD, "An improved spray model for reducing numerical parameter dependencies in diesel engine CFD simulations," SAE Technical Paper 2008-01-0970, 2008.
19. Yue Z, Hessel RP, Reitz RD, "Investigation of real gas effects on combustion and emissions in internal combustion engines and implications for development of chemical kinetics mechanisms," International J. of Engine Research, Vol. 19, Issue 3, Pages 269-281, 2017.
20. Siebers DL, "Scaling liquid-phase fuel penetration in diesel sprays based on mixing-limited vaporization." SAE Technical Paper 1999-01-0528, 1999.
21. Rowley RL, Wilding WV, Oscarson JL, Yang Y, Zundel NA, Daubert TE, Danner RP. "DIPPR data compilation of pure compound properties." Design Institute for Physical Properties. 2003.
22. Qiu L, "Development of a phase stability-based fuel condensation model for advanced low temperature combustion engines." PhD Dissertation, University of Wisconsin–Madison, Madison, WI, 2014.

23. Qiu L, Wang Y, Jiao Q, Wang H and Reitz RD "Development of a thermodynamically consistent, robust and efficient phase equilibrium solver and its validations." Fuel 2014; 115: 1–16.
24. Qiu L, Reitz RD, "Simulation of supercritical fuel injection with condensation." Int. J. Heat Mass Tran 2014, 79, 1070–1086.
25. Qiu L, Reitz RD, "Investigating fuel condensation processes in low temperature combustion engines." J. of Engineering for Gas Turbines and Power 2014; 137(10): 101506.
26. Qiu L, Reitz RD, "An investigation of thermodynamic states during high-pressure fuel injection using equilibrium thermodynamics." Int. J. Multiphase Flow 2015; 72:24–38.
27. Amsden AA, "KIVA-3V, Release 2: Improvements to KIVA-3v." LA report, Report no. LA-UR-99-915, 1999.
28. Perini F, Galligani E, Reitz RD, "An analytical Jacobian approach to sparse reaction kinetics for computationally efficient combustion modeling with large reaction mechanisms." Energy Fuels 2012; 26 (8): 4804–4822.
29. Wang H, Yao M, Yue Z, Jia M, Reitz RD, "A reduced toluene reference fuel chemical kinetic mechanism for combustion and polycyclic-aromatic hydrocarbon predictions," Combustion and Flame, Vol. 162, 2015, pp. 2390–2404.
30. Wang BL, Miles PC, Reitz RD, Han Z, Petersen B, "Assessment of RNG Turbulence Modeling and the Development of a Generalized RNG Closure Model," SAE Technical Paper 201101-0829, 2011.
31. Babajimopoulos A, Assanis DN, Flowers, D L, Aceves, S M, Hessel, RP. "A fully coupled computational fluid dynamics and multi-zone model with detailed chemical kinetics for the simulation of premixed charge compression ignition engines." International Journal of Engine Research, 6(5), 497–512 (2005). https://doi.org/10.1243/146808705X30503
32. Reynolds WC, Parekh DE, Juvet PJD, Lee MJD, "Bifurcating and Blooming Jets," Annual Review of Fluid Mechanics 2003 35:1, 295-315
33. Skeen S, Manin J, Pickett L, "Visualization of Ignition Processes in High-Pressure Sprays with Multiple Injections of n-Dodecane," SAE Technical Paper 2015-01-0799 (2015).
34. Chishty, M, et al., "A Numerical Study of Spray A with Multiple-Injections Using the Transported PDF Method," 10th Asian-Pacific Conference on Combustion, July 2015.

Appendix A

Gas-jet model details

One may ask how to derive the transient axial velocity field, $\boldsymbol{u}$, to use in Equation (2)? The gas-jet model is based on the valid assumption that a jet forms similarly when driven by a liquid spray, or by an inflow of turbulent gas, as long as the mass and momentum 'injected' in both scenarios are the same [13-15]. The jet formed according to turbulent gas jet theory that represents a spray of equal mass and momentum flowrate is achieved when the gas flow has an effective diameter, $d_{gas-jet} = d\sqrt{\rho_d/\rho_g}$, and the same initial velocity as the spray. The axial velocity field at axial location x and radial location r, at time t is then given as a sub-grid velocity, $\boldsymbol{u}_{sgs}$, given by Equation (12), [16].

$$\boldsymbol{u}_{sgs}(x,r,t) = \frac{f(\chi)\boldsymbol{u}_{eff}(x,t)}{\left(1+\frac{12r^2}{{K_{entr}}^2x^2}\right)^2} \tag{12}$$

$$f(\chi) = \begin{cases} 1/\chi & \chi \geq \varphi \\ \gamma_{max} - \frac{32{\gamma_{max}}^3(\chi-1)^2}{(3+\Delta)^2(3+\Delta-4\gamma_{max})} & 1 \leq \chi < \varphi \\ \gamma_{min} + \chi(2-\chi)(\gamma_{max}-\gamma_{min}) & \chi < 1 \end{cases} \tag{13}$$

$$\chi = xK_{entr}/\left(3d_{gas-jet}\right) \tag{14}$$

$$\Delta = \sqrt{9-8\gamma_{max}} \tag{15}$$

$$\varphi = (3+\Delta)/(4\gamma_{max}) \tag{16}$$

$$\boldsymbol{u}_{eff}(x,t) = \boldsymbol{U}_{inj}(t_0) + \sum_{k=1}^{n}\left(\left(1-exp\left(-\frac{t-t_k}{\tau(x,t_k)}\right)\right) \times \left(\boldsymbol{U}_{inj}(t_k)-\boldsymbol{U}_{inj}(t_{k-1})\right)\right) \tag{17}$$

[12]

$$\tau(x,t) = St\cdot x/\left|\boldsymbol{U}_{inj}(t)\right| \tag{18}$$

$\boldsymbol{u}_{eff}(x,t)$	Effective axial velocity at location x and time t.
$K_{entr} = 0.85$	Turbulent entrainment coefficient [16].
$\gamma_{max} = 0.7$	Axial damping profile coefficients [16].
$\gamma_{min} = 0.6$	
$\boldsymbol{U}_{inj}(t_k)$	Injection velocity at time t_k.
n	The number of times $\boldsymbol{U}_{inj}$ changes.
$\tau(x,t_k)$	Jet response time.
$St = 3.0$	Stokes number [12].

The gas jet model [16,17,18] has performed well under conditions similar to the conditions of this study; i.e., low-temperature, cool-flame [17] and conventional-diesel combustion [19].